Low friction and wear resistant coatings

Carvalho, Nuno Jorge Marcolino

3

MICROSTRUCTURE OF *WC/C* MULTILAYERS

3.1 INTRODUCTION

New trends in mechanical engineering are leading to more stringent requirements on machine components. For example, the reduction of friction to increase the efficiency of motors, the improvement of the reliability of gears and roller bearings, and the reduction of hazardous lubricants are of major concern in the design of machinery. These trends might cause higher tribological stresses on components because higher loads, closer tolerances or the reduction of lubricant can lead to adhesive wear of surfaces. One way to cope with these trends is to improve the surface properties by applying a thin low-friction high-wear-resistance solid film onto the machine components. Among others, molybdenum sulphide,[1,2] and diamond-like carbon (DLC) have shown the most promising results.[3-5] The main properties of these coatings include low static and dynamic friction coefficients against most metals and ceramics, chemical inertness, resistance to corrosive attack in acid or saline media, and high wear resistance.

DLC coatings are amorphous and consist of a mixture of sp^3 and sp^2 carbon structures, where sp^2-bonded graphite-like clusters are embedded in an amorphous sp^3-bonded carbon matrix.[6] They have been subject to studies since the 1970's and several different types of DLC have emerged. The most

noteworthy are: pure DLC, hydrogen-free (i-C), hydrogenated (a-C:H), and metal-doped or carbide-doped (Me-C:H) amorphous carbon coatings. The dissimilarity between hydrogen-free and hydrogenated films consists in the proportion of sp^3 bonds, being 85 to 95% for hydrogen-free and 30 to 60% for hydrogenated. It is believed that the presence of hydrogen atoms play a crucial role in the bonding configuration by promoting and stabilising sp^3 tetrahedral bonds of the carbon atoms, which is suggested by some authors to be the origin of the high hardness of DLC coatings.[7,8]

Metal-doped and carbide-doped DLC have received considerable attention in recent years, owing to their low friction coefficient and high wear resistance in combination with substrate temperatures of some 200-400 ^oC during deposition. Further, the fact that adhesion between the coating and the substrate has been improved by depositing an interlayer of chromium or molybdenum,[9] has helped to promote the deposition of such coatings onto machine components subjected to a high shear stress component. Tungsten carbide/carbon (WC/C) is an example of a multilayers structure composed by carbide-doped hydrogen and hydrogenated DLC lamellae. This coating has been reported to have successful engineering applications where low friction and high wear resistance are important requirements.[10,11] However, if the advantages are to be fully employed in improving the surface properties of engineering components, it is necessary to understand more thoroughly the detailed mechanisms by which surface properties are improved.

Chapter 3 addresses the chemical composition, microstructure and interfaces of several WC/C coatings. Moreover, the predominant features of and dissimilarities between the different films, which can be crucial for their performance, will be pointed out throughout the text.

Transmission electron microscopy (TEM) - in conventional and high-resolution mode - was used as primary technique. All images were acquired close to the minimum contrast defocus. The difference observed between this defocus value and the optimum defocus consisted only on the granularity (noise) of the amorphous material. Since it was much coarser at the optimum defocus, the former value was adopted throughout. By combining direct imaging and electron diffraction, it was possible to obtain detailed information about phase

composition, grain size and shape, and degree of preferred orientation of the crystalline phases. Nevertheless, complementary techniques such as analytical TEM, scanning electron microscopy (SEM), X-ray diffraction (XRD), and Auger electron spectroscopy (AES) were also used, providing additional invaluable information concerning the morphology, phase composition, and microchemistry of the coated systems.

3.2 COATED SYSTEMS

In this thesis three dissimilar WC/C coatings - denoted S1, S2, and T1 - were investigated. Stainless steel (AISI 304) and tool steel (AISI D2) were used as substrate materials, having both a circular (60 mm external diameter, 13 mm thick) and a rectangular (90x10x1.5 mm) geometries. The tools steel substrate was heat treated and tempered at 520 °C to obtain a hardness of 60 HRc (6.8 GPa). The substrate surfaces were finished by polishing to an average roughness, R_a, of 0.03, 0.05 and 0.07 µm. The substrate properties of the coated systems are summarised in table 3.1.

Table 3.1 *Substrate properties of the coated systems*

Sample ID	Substrate material	Substrate hardness H_V [GPa]	Substrate roughness R_a [µm]
S1	Stainless steel (AISI 304)	1.6	0.05
S2	Stainless steel (AISI 304)	1.6	0.03
T1	Tool steel (AISI D2)	6.8	0.07

3.3 PHASES AND CRYSTAL STRUCTURE

From XRD analysis, it was found that all coatings investigated consist of a cubic and an amorphous phase. The diffraction peaks detected in XRD patterns are displayed in figure 3.1. In the case of coating systems S1 and T1 the chromium (110) lattice plane provided the most intense peak, whilst in system S2 both the (110) and (200) planes were most intense. Therefore, the chromium interlayer of systems S1 and T1 has a (110) preferred orientation parallel to the surface, whereas system S2 does show two possible orientations, (110) and (200). All systems displayed a broad peak characteristic of an amorphous phase suggesting that both WC and carbon layers are amorphous. The only exception is in the system T1 where a single diffraction peak indicates the presence of a WC crystalline phase.

The morphology of the WC/C is disclosed by plan-view and cross-sectional SEM micrographs in figure 3.2. The coatings have a nodular surface morphology with growth defects - droplets - typical for PVD.[12] Their morphological difference is mainly based on the density of small droplets originating from the deposition process. It is thought that the increased droplets density observed in coating S2 was caused by slightly decreasing of either the bias sputtering (bias voltage applied during ion bombardment in planar sputtering apparatuses) or working gas pressure. Both parameters are reported[13] to lower the ion energy of the atoms impinging upon the growing surface. Consequently, the effectiveness of the ions in suppressing the formation of droplets by sputter redistribution of coating material during growth was reduced.

The surface grooves in the coating are due to irregularities on the underlying substrate, as can be attested by the cross-sectional micrographs. The substrate irregularities, grooves and ridges, were still present after the pre-treatment because the process was unidirectional. The polishing resulted in a smoother surface. However, it did not remove completely the deeper grooves or higher ridges. The coating thickness and surface roughness are presented in table 3.2. The cross-sectional SEM micrographs were obtained with a backscattered electron (BSE) detector. Since the number of BSE increases with increasing atomic number, figures 3.2b, 3.2d, and 3.2f revealed important insights

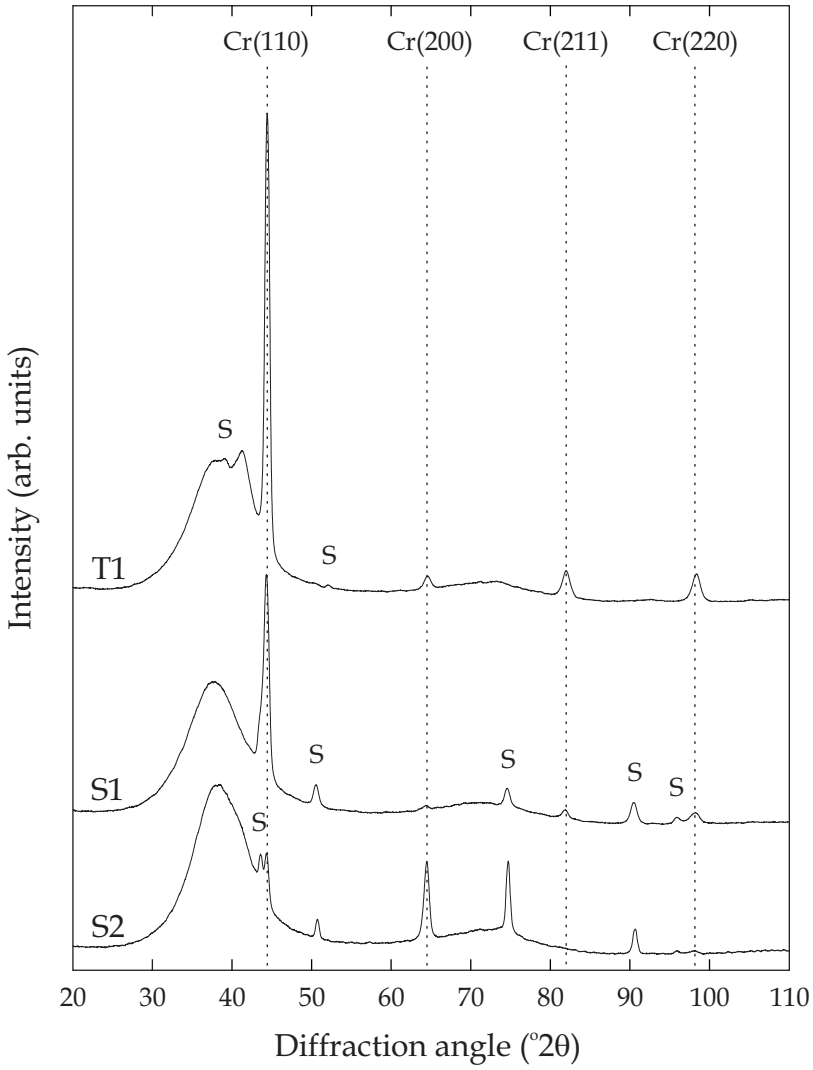

Figure 3.1 *X-ray diffraction patterns of coated systems T1, S1, and S2. The reference positions of body centred cubic chromium phase and peaks from the steel substrates (labelled S) are indicated. The diffraction pattern of stainless steel consists mainly of γ-Fe and Fe-Cr-Ni phases, while tool steel consists of α-Fe and chromium carbide, Cr_7C_3, phases.*

regarding the coatings composition. Apparently, the concentration and distribution of tungsten, the element with higher atomic number, is different in the various coatings. Systems S1 and T1 are alike with respect to the thickness of the band with a higher tungsten concentration, whereas in system S2 the

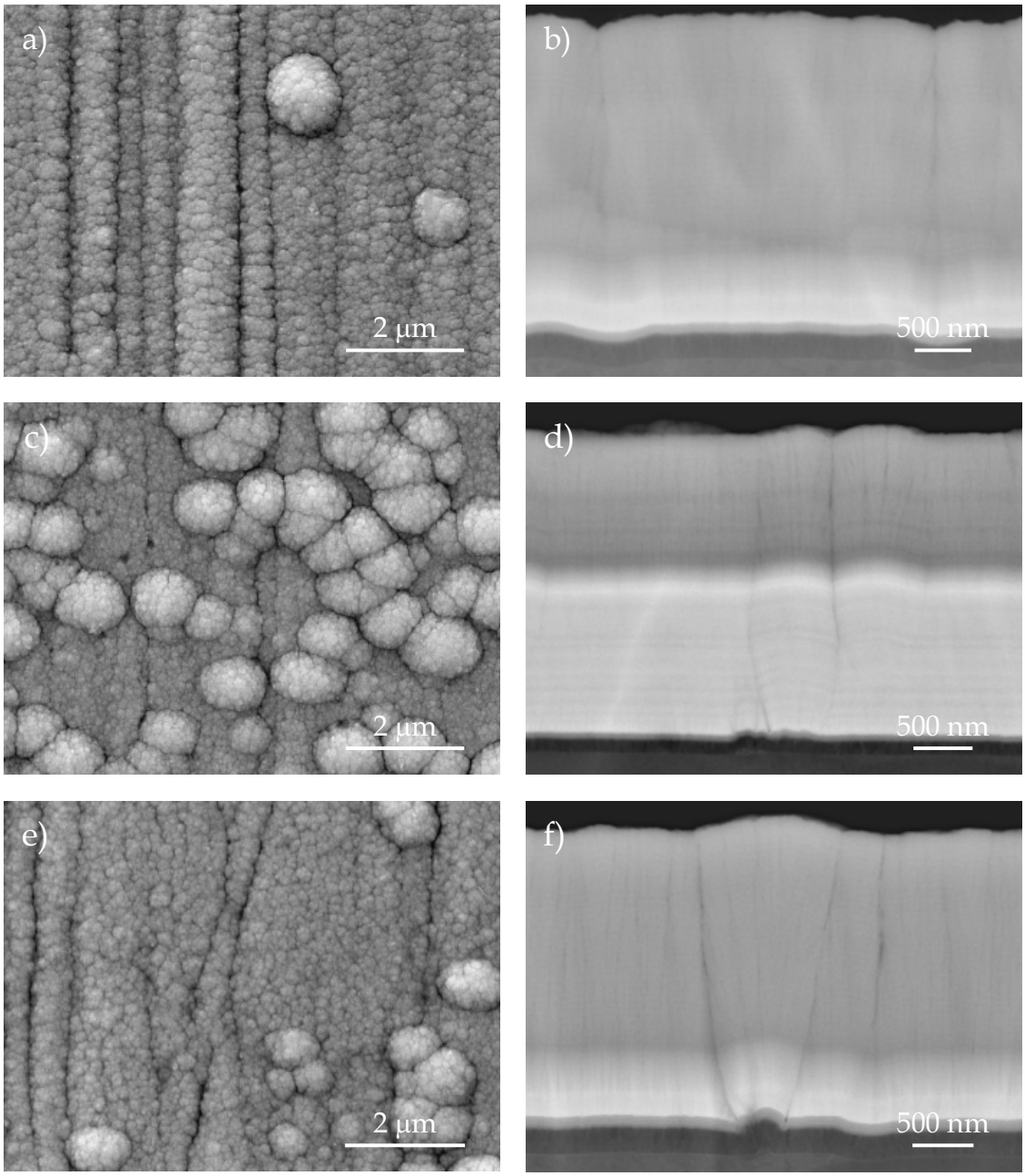

Figure 3.2 *SEM micrographs displaying the morphology of WC/C coatings:* (a) *and* (b) *plan-view and cross-section from coated system S1, respectively;* (c) *and* (d) *micrographs from system S2;* (e) *and* (f) *micrographs from system T1. The plan-view micrographs illustrate the coating nodular surface morphology, typical of PVD process and grooves created by underlying substrate irregularities. The cross-sectional micrographs obtained with backscattered electron detector show differences in tungsten concentration.*

band is roughly twice as thick. As can be promptly perceived this difference may have a direct influence on the elastic properties of the coating.

The tungsten enrichment of the brighter band observed in BSE micrographs was cross-checked by an AES line profile. This technique was utilised on a cross-sectional sample from system T1, prepared as described in chapter 2. Figure 3.3 shows such AES line profile. It can be seen that both C and Cr Auger intensities are enhanced at the Cr layer. After that, the W intensity increases reaching a maximum in the brighter band, while for C it is the opposite. The Cr drops to zero, indicating that the Cr deposition ceased. EDS analysis performed on cross-sectional TEM specimens, also confirm the W and C concentration gradient at the WC layer. However, beyond this region their intensities are uniform through the remaining multilayer until roughly half a micrometer from the top. From here on, the friction properties of the film are enhanced by an increase of C and decrease of W. The sharp C signal at the edge of the sample is related to a change in surface orientation of the sample (edge of the cross section) rather than a sudden increase in concentration.

Table 3.2 *Total coating thickness and surface roughness.*

Sample ID	Coating thickness [µm]	Coating roughness R_a [µm]
S1	3	0.05
S2	2.8	0.05
T1	2.7	0.06

The coating-substrate interface is shown by a HRTEM image in figure 3.4. There is an amorphous interfacial region (approximately 5 nm thick) between the crystalline steel substrate and the columnar chromium. The interphase shows a relatively smooth top surface, whereas the interface to the underlying steel presents a slight roughness due to diffusion of chromium into steel. From a through-focal series of images it was learned that the interphase showed no

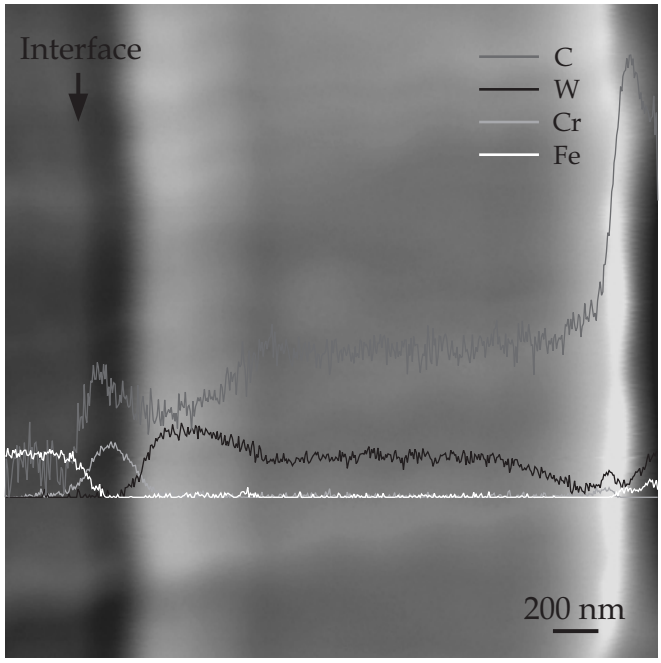

Figure 3.3 *Line profile of C_{KLL}, W_{MNN}, Cr_{LMM}, and Fe_{KLL} Auger intensity plotted as a function of film thickness. The data, presented as measured, is superimposed on a SEM micrograph of the coated system T1. The zero intensity line corresponds to the position where the data was taken. The arrow indicates the coating-steel interface.*

contrast reversal, i.e. the contrast did not change from bright to dark as the focus condition was changed from under- to over-focus. This indicates that the interfacial region is made up of a high-atomic-density phase.[14] It is believed that this high density interfacial contact allows a robust adhesion of the chromium layer to the substrate. Further, the interphase initially has a higher contrast, suggesting that it is composed by a higher mass-thickness. All these considerations allow to assume that first chromium had diffused into the steel, to an extent of ~2.5 nm, and then an amorphous chromium region was formed. Within this amorphous layer the columnar structure must have been nucleated.

Figures 3.5a, 3.5b, and 3.5c are plan-view TEM images, with corresponding SAED patterns, from coatings S1, S2, and T1, respectively. The images clearly demonstrate that the coatings, at least the upper part from where the images were taken, are amorphous. However, a medium-range order is present with an

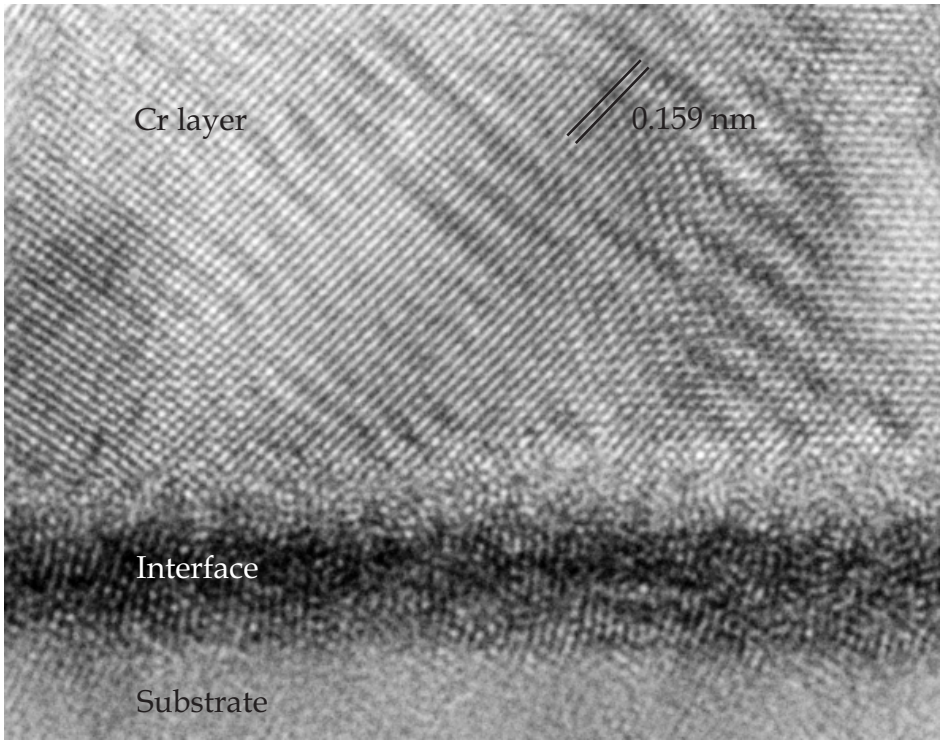

Figure 3.4 *Cross-sectional HRTEM image of the coating-substrate interface region of coated system T1. The other systems interphase are similar to this one.*

approximate average domain size of 3 nm in coatings S1 and S2, and 10 nm in T1. This type of microstructure has been described as a uniform three-dimensional network structure.[15] Accordingly, these coatings are composed of a mixture of sp^3- and sp^2-bonded carbon atoms. The sp^2- bonding, from energetic considerations and propensity to form planar ring and sheet structures, tend to segregate in small graphitic clusters containing fused sixfold rings, which are embedded within a sp^3-bonded random network. Further, it is reasoned that the granular structure seen in the images is related to strain, rather than to the percolating patterns of sp^2 and sp^3 bonds. The strain in the structure instead of being distributed randomly is relieved abruptly at the edges of the sp^2-islands creating the difference in contrast.[16] Nevertheless, in coating T1 (figure 3.5c), due to the larger cluster size, most likely caused by a lower hydrogen content, the strain relieve was more homogeneous.

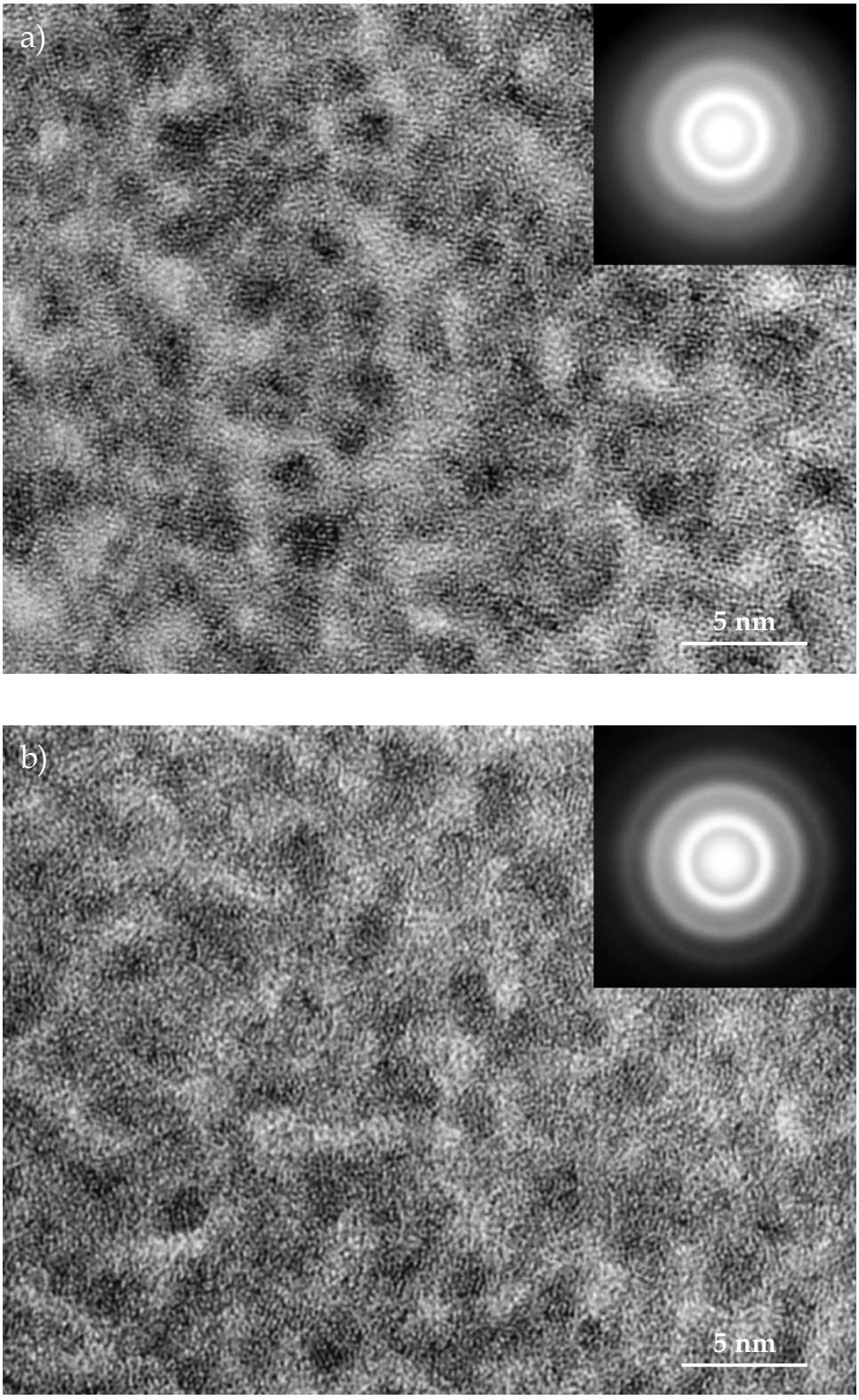

Figure 3.5 *(caption on facing page)*

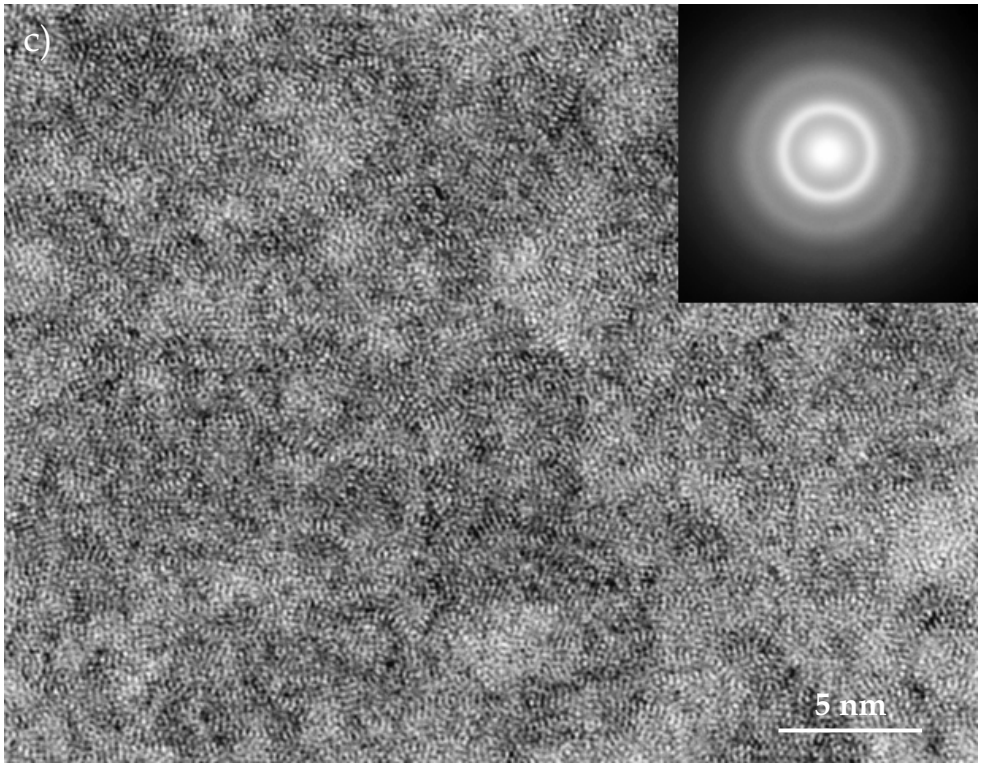

Figure 3.5 *Plan-view TEM images exhibiting the planar microstructures of the coatings:* (a) *system S1;* (b) *system S2;* (c) *system T1. The SAED patterns are identical and indicative of an amorphous phase.*

The SAED patterns shown in the insets are identical and composed of diffuse diffraction rings typical of amorphous materials. The two most intense diffraction rings were observed to have an interplanar spacing of 0.245 nm and 0.140 nm, which is consistent with previous reports.[17] The measured interplanar spacing of these two rings reinforces the idea of a diamond like structure, considering that for crystalline diamond the (111) and (220) strongest reflections correspond to d=0.206 and 0.126 nm, respectively.

The microstructure of the coating systems is presented by overview cross-sectional TEM images in figure 3.6. Their structure, when going from the interface with the substrate to the surface of the coating, is formed by a chromium interlayer, intermultilayers of WC and carbon, a WC layer, and finally the WC/C multilayers.

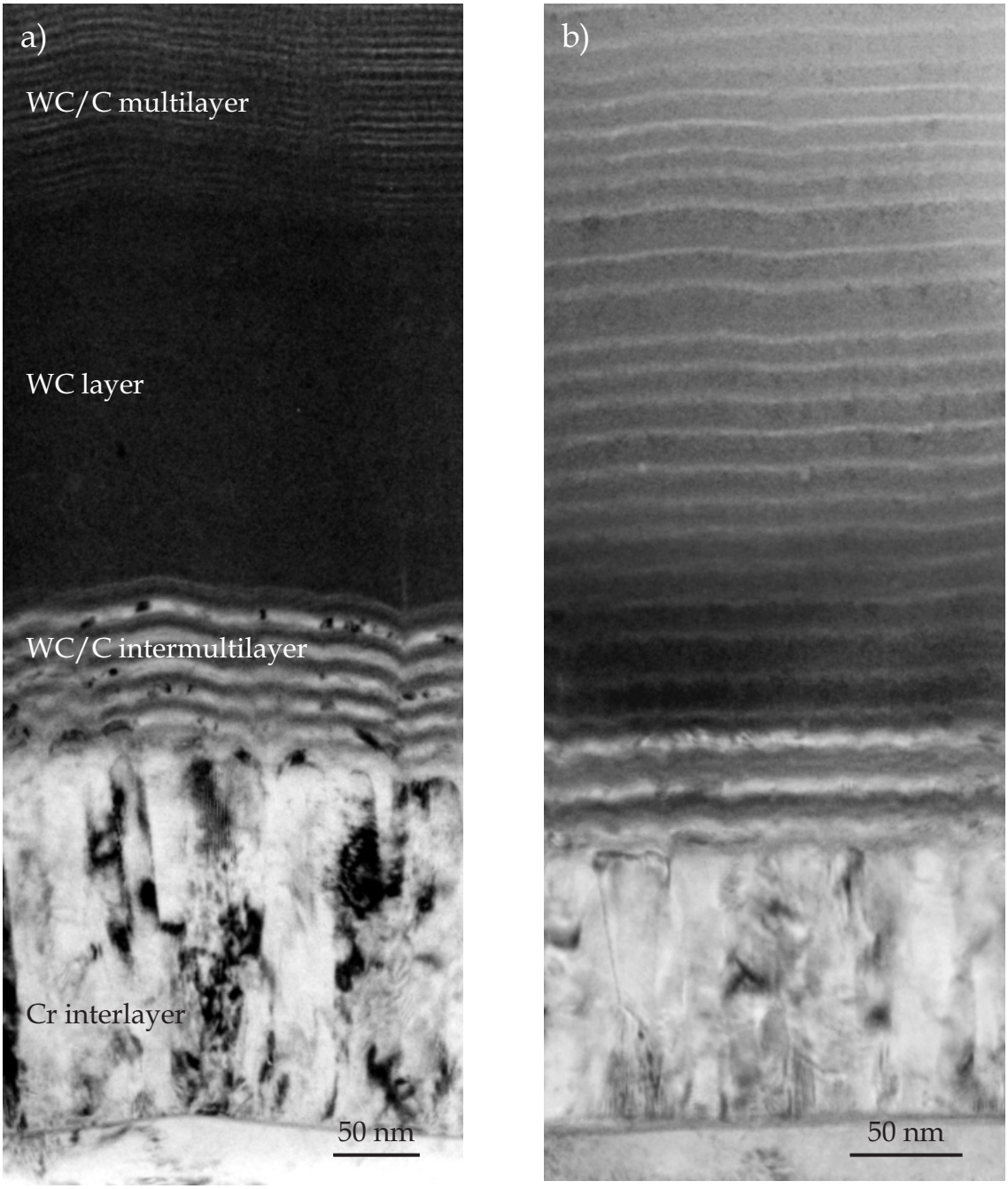

Figure 3.6 *(caption on facing page)*

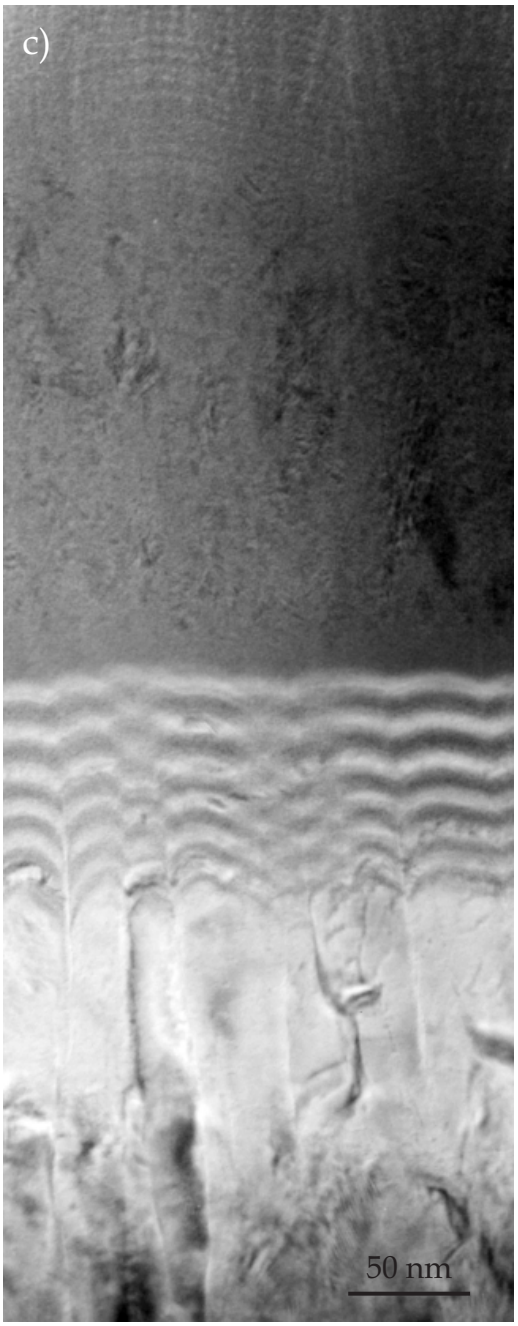

Figure 3.6 *Cross-sectional overview TEM images showing the microstructure of the coatings:* (a) *system S1;* (b) *system S2;* (c) *system T1. The structure is constituted of a chromium interlayer, an intermultilayer, a WC layer for systems S1 and T1, and the WC/C multilayers.*

The chromium interlayer has a dense columnar structure, typical of coatings grown under low energetic ion bombardment and limited adatom mobility conditions.[18] Their average thickness is ~205 nm, except in system S2 which thickness is ~120 nm. The average column diameter is 22, 18, and 24 nm for system S1, S2 and T1, respectively. This indicates that the columns broaden

with increasing layer thickness. Therefore, the column diameter can be explained considering the three stages of development of textures in PVD films: nucleation, competitive growth, and steady growth. Once the (110) orientation achieved dominance in the competitive growth at the expenses of the (200) orientation (cf. figure 3.1), which is thought to occur after the first 100 nm, the interlayer grew steadily with this preferred orientation.

The intermultilayers are fashioned by WC and carbon amorphous layers, corresponding to darker and brighter bands, respectively. Their thicknesses in system S1 and T1 are ~93 nm with a periodic wavelength, Λ, of ~15.5 nm. On the other hand, in system S2 they are ~50 nm thick. Further, their structure is different, comprising of three thicker carbon layers with thinner WC and carbon lamellae in between. The chromium columnar structure seems to have grown into all the intermultilayers distorting them by imposing a wavy structure with a period linked to the column diameter. As a result, nano-polycrystalline particles of chromium carbides were formed in the carbon layers.

In between the intermultilayer and the WC/C multilayers there is an amorphous WC layer with a thickness of ~200 nm in system S1 and T1. In the former, the layer is truly amorphous while within the latter polycrystalline columnar particles were grown. In addition, this layer is darker than the remaining coating, indicating that it has a higher mass-thickness. Altogether, these interfacial bond layers between the WC/C multilayers and the substrate are employed to provide a good adherence in applications where a high shear stress component is present.[11]

The WC/C multilayers have an interlaminar structure with the darker lamellae being WC rich and the brighter lamellae carbon rich. Once again, the thickness of the interlaminants in systems S1 and T1 are roughly the same, ~6 nm for WC and ~2 nm for carbon. In the case of system S2, they were grown directly on the intermultilayers with a Λ of ~15.5 nm, and a WC lamella thickness of ~13 nm.

From HRTEM, it was found that the multilayers have a different interlaminar structure (see figures 3.7a and 3.7b). In systems S1 and T1, they consist of an amorphous phase, whereas in S2 are constituted of an amorphous matrix with clusters of crystalline particles embedded in the WC lamellae. The carbon lamellae have approximately the same thickness in the three coatings. However,

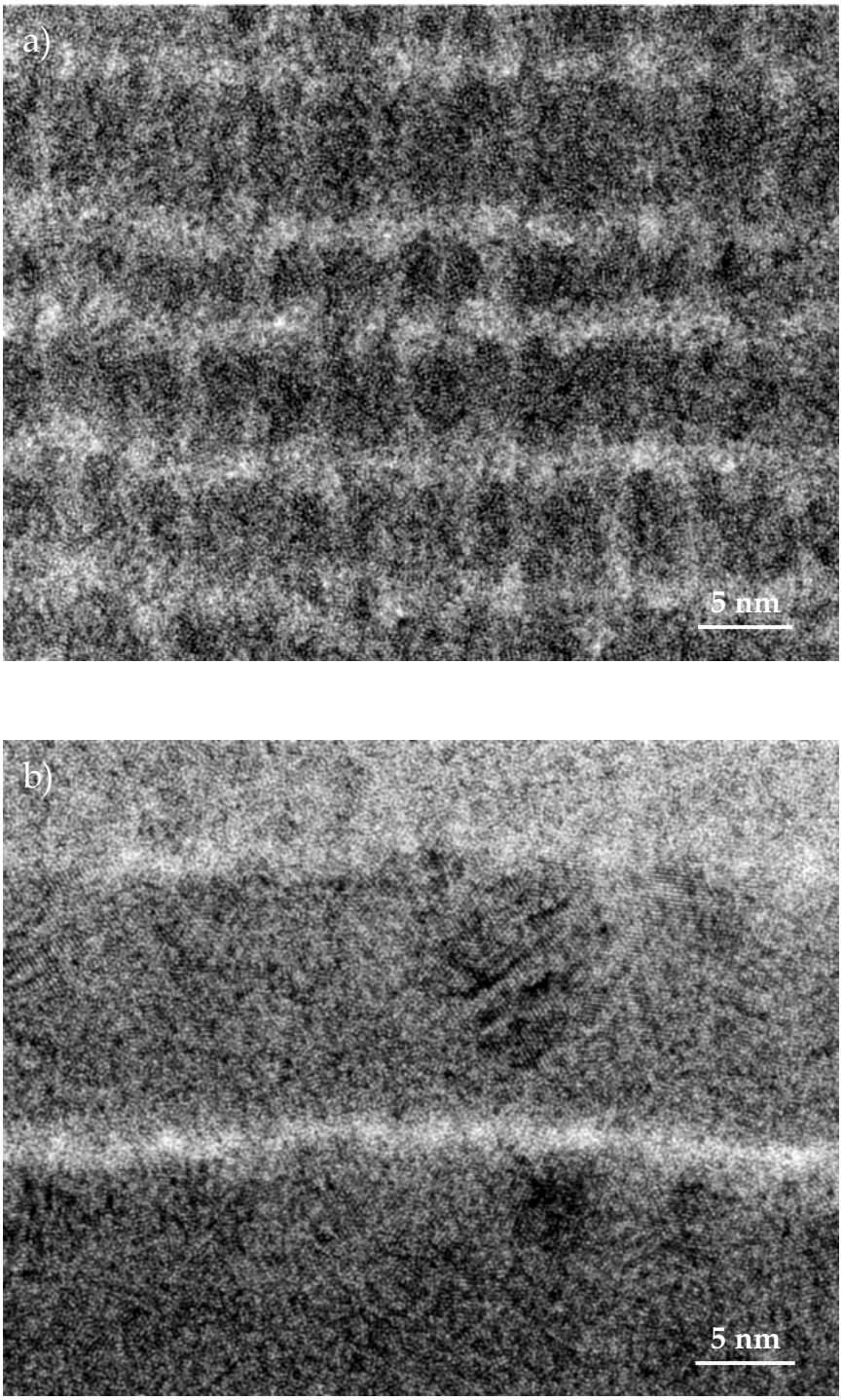

Figure 3.7 *Cross-sectional HRTEM images of the interlaminar structures:* (a) *coated system S1 displaying the diffuse C-WC interface (the one from system T1 is similar);* (b) *coated system S2 with a sharp C-WC interface. On both images the brighter lamellae correspond to carbon.*

the C-WC interface in the former systems is rather diffuse, whereas in S2 the interface is sharper. As mentioned before, the possible lower bias sputtering employed during the deposition of coating S2 resulted in a weaker atomic mixing at the interface. This created a sharper interface with a reduced bonding between the lamellae. An overview of the constitution and dimensions of the coated systems is given in appendix 3.1.

3.4 PARTICLES EMBEDDED IN AN AMORPHOUS STRUCTURE

The structure of the intermultilayers consists of WC and carbon layers, both being amorphous. However, in the latter, nano-polycrystalline particles were found. An example of such particles is shown in figure 3.8. As can be observed, the structure of the layers depends on the interface roughness originating from the individual chromium columnar structure. It is interesting to note, that the shape of the polycrystalline particles follow the morphology of the carbon layers and are only present in these ones. The formation of these particles can be attributed to some residual chromium atoms that might still be present in the coating chamber after the interlayer growth, and due to their high affinity for carbon, chromium carbide nano sized particles have been formed. This assumption is supported by electron energy filtered images of the intermultilayers, where chromium was mapped in the carbon layers.

Another type of crystalline particles, embedded in the amorphous WC layer of system T1, is disclosed in figure 3.9a. These particles prevailed throughout the layer and have a structure similar to the ones formed by ballistic aggregation on a point seed.[19] However, the void streaks often observed in the columnar structure, were replaced here by stacking faults. The growth direction of the particles was parallel to the <200> direction and normal to the coating-substrate interface.

From selected area electron diffraction pattern analysis, it was possible to identify the structure of these particles as face centred cubic β-WC_{1-x}. This identification is also in agreement with the XRD pattern, where the diffraction peak unidentified in figure 3.1 corresponds to the (200) plane of the β-WC_{1-x} phase. As can be seen in the HRTEM image of figure 3.9b, the crystal has a high

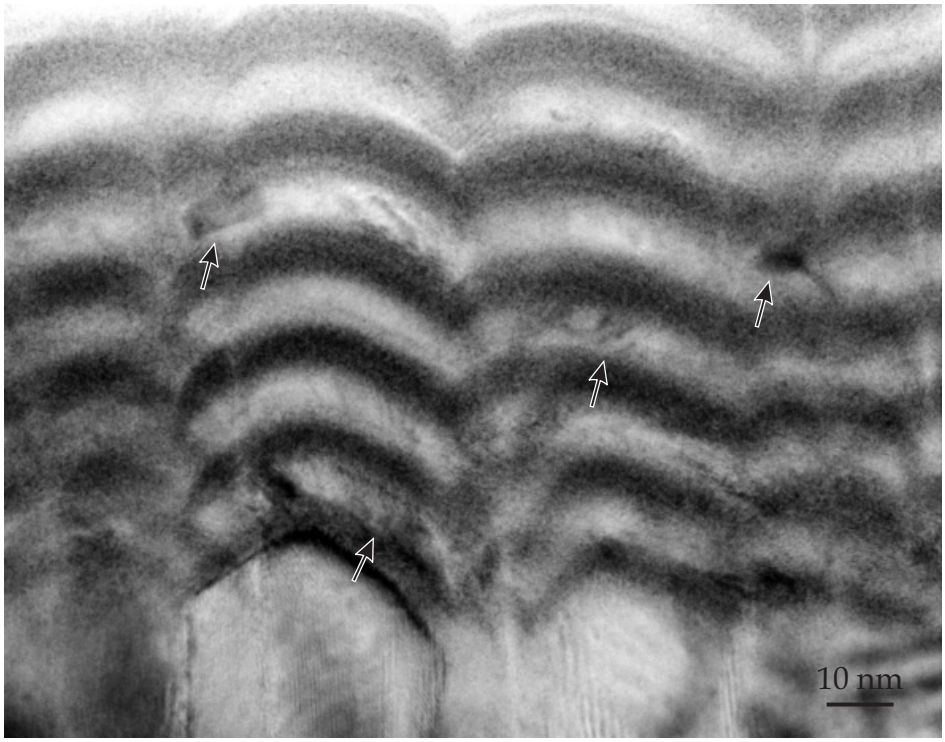

Figure 3.8 *Cross-sectional TEM image of the intermultilayers of coated system T1. The darker layers correspond to WC, whereas the brighter correspond to carbon. In the latter, nano-polycrystalline chromium carbides are present due to growth of chromium into the intermultilayers (some are arrowed). Moreover, the morphology of the intermultilayers is related to the diameter and top morphology of the chromium columns. Planar defects were created at the interface of the columns whenever the columns presented a faceted top morphology.*

density of stacking faults in the {111} planes. This fact, is related to the cubic β-WC_{1-x} phase being stable only for a carbon concentration of ~40 at%, while for higher carbon content the hexagonal structure is more favourable.[20] Nevertheless, microchemical analysis performed by EDS showed that the particles present in the amorphous layer have an atomic concentration of carbon related to their hexagonal structure. Therefore, the presence of intrinsic stacking faults in the close packed {111} planes allows local transformations of the cubic structure into hexagonal.

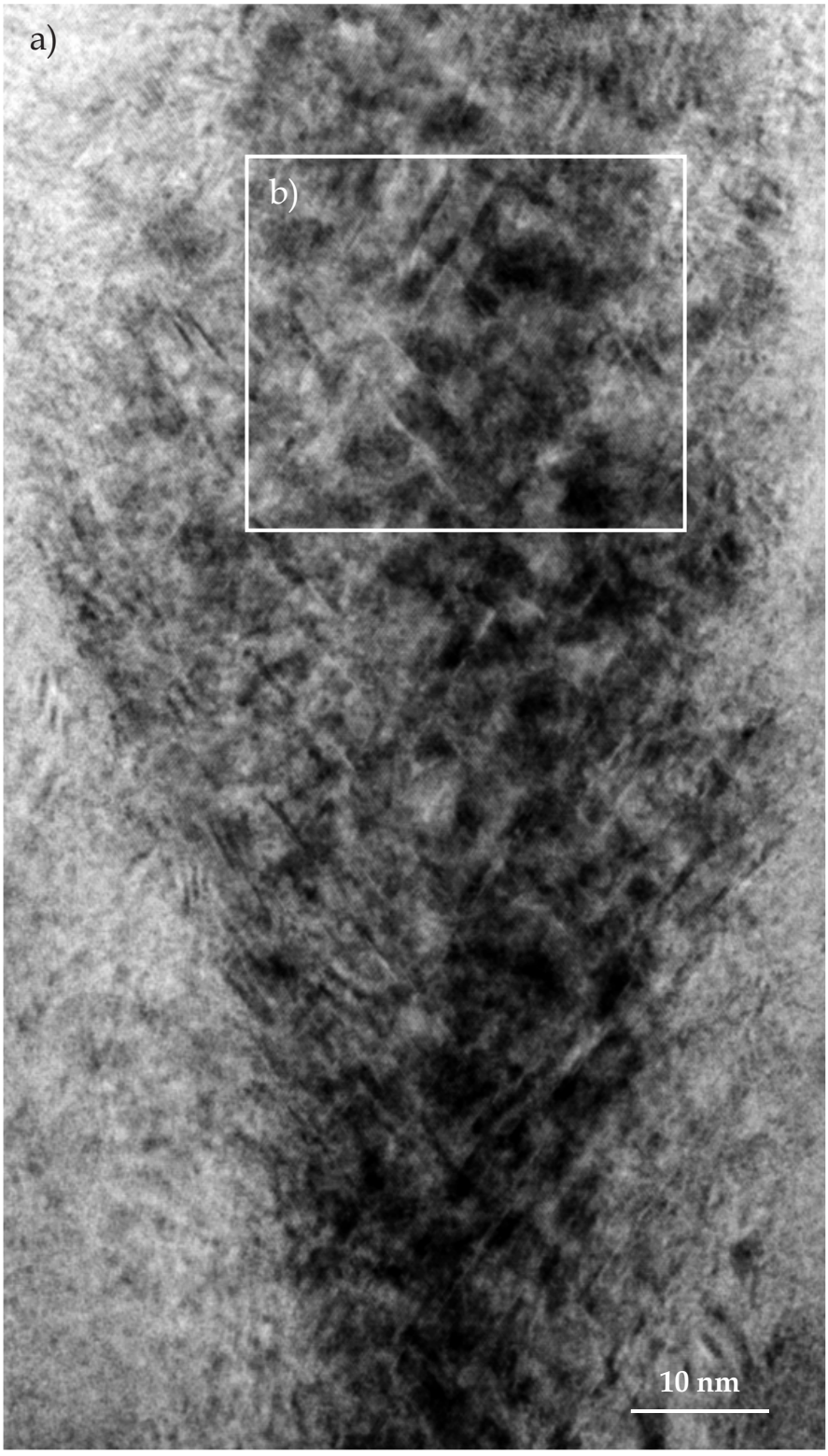

Figure 3.9 *(caption on facing page)*

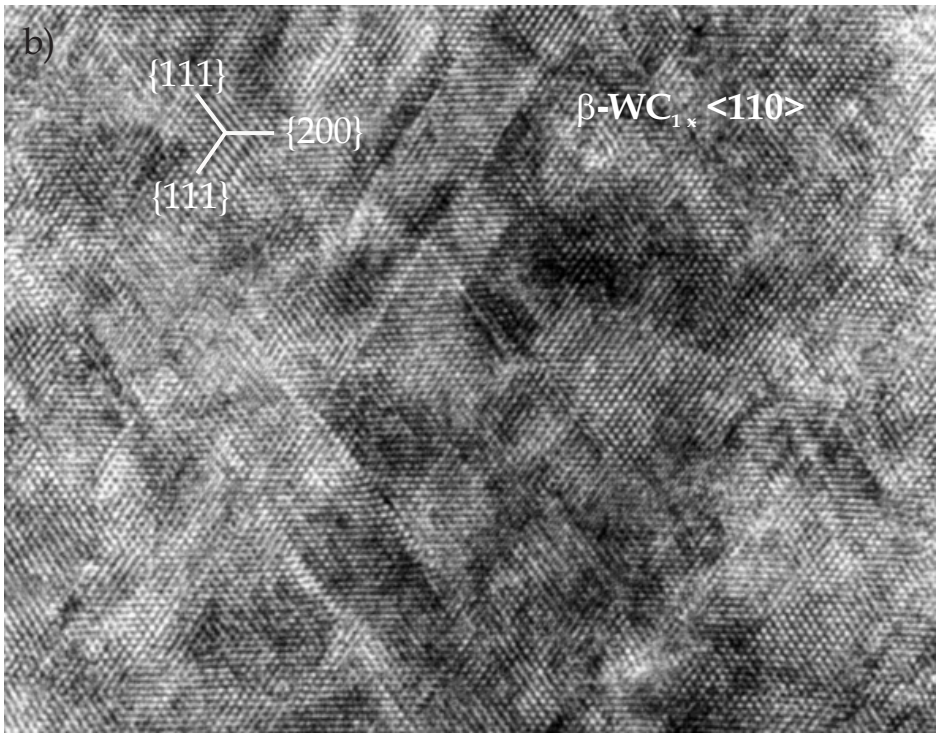

Figure 3.9 *Cross-sectional TEM image of* (a) *a crystalline columnar particle embedded in the amorphous WC layer from coated system T1. The particle is viewed along the <110> zone axis and was identified as having a cubic* β-WC_{1-x} *phase.* (b) *HRTEM image showing the intrinsic stacking faults in the {111} planes of the particle.*

The WC/C multilayers from coating system S2 are constituted by an amorphous interlaminar structure with clusters of crystalline particles entrenched in the WC lamellae. Figure 3.10 shows a HRTEM image of a WC lamella containing such nano-crystalline particles. They are equally distributed throughout the multilayers, having a relatively constant diameter of 4 to 10 nm. Their position in the lamella is always shifted slightly towards the upper part. This observation, allows to assume that their nucleation did not occur at the first WC atomic layers because the interface with the previous carbon lamella was not sharp, owing to interdiffusion of the latter. Therefore, as the particles nucleation started roughly in the middle of the lamella and it was ceased by the growth of the next carbon lamella, they have obviously, a smaller size than the lamellae thickness. Given their relatively small size it was impossible to

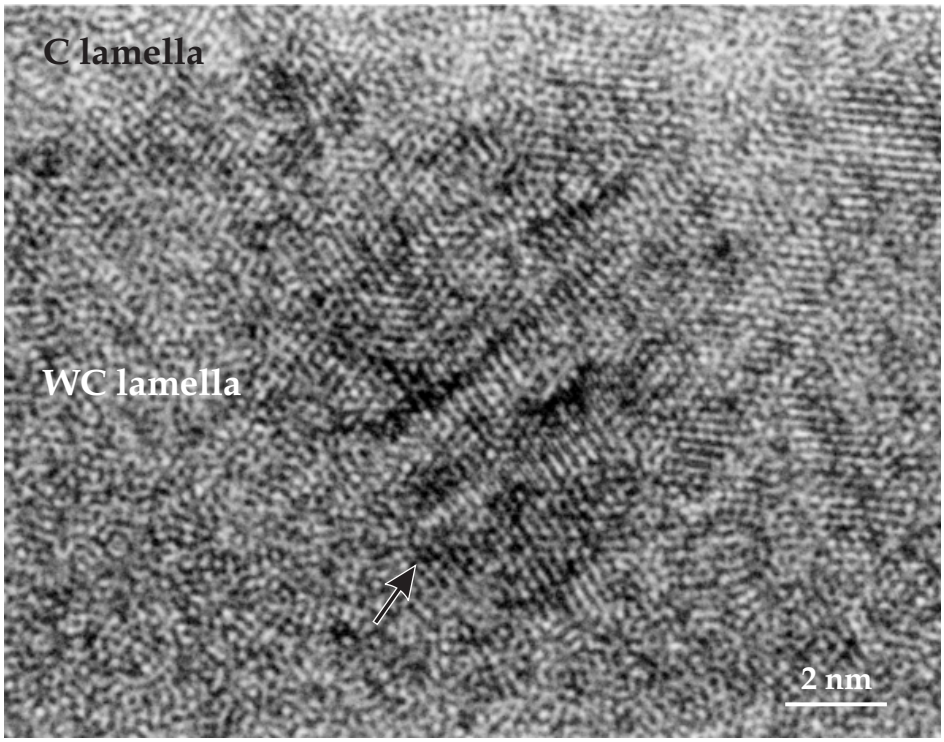

Figure 3.10 *Cross-sectional HRTEM image of the interlaminar structure from coated system S2, exhibiting the nano-crystalline clusters embedded in the WC rich lamella. The carbon rich lamella is represented on top of the image by the brighter stripe. The arrow marks the position of a nano-crystalline cluster identified as having the cubic β-WC_{1-x} phase.*

determine the crystal structure and hence the phase either by XRD analysis or selected area electron diffraction. Thus, to calculate the structure of the clusters, Fourier transformation from the HRTEM images was applied to obtain the diffraction pattern. Subsequently, the diffraction pattern was rotated to get rings from the symmetrically distributed diffraction points, and the interplanar spaces corresponding to the lattice points were measured. The same method was applied to the crystals present in the WC layer from system T1, and both were compared. The result allowed to conclude that the clusters present in the WC lamellae of system S2 have the same phase - cubic β-WC_{1-x} - as the crystals present in the WC layer of system T1. In the other coating systems, the WC

lamellae have no particles present, which is believed to be related to their reduced thickness of ~6 nm not enabling particle nucleation and growth.

3.5 DEFECT STRUCTURE

The coated systems exhibited two types of defects that are prone to jeopardise their mechanical properties. They were induced either by substrate surface irregularities or simply by the top morphology of the chromium columns. The defects produced by the substrate ridged surface were transferred through and magnified by the coating. Their growth structure was a direct consequence of the geometric shadowing because the high points on the growing surface received more coating flux than the valleys.[21] Moreover, the application of low energy ion bombardment with a small fraction of resputtering did not allow the production of planar surfaces. Thus, macroboundaries (defects) developed at the lower chromium surface within a groove, and at either side of a ridge (cf. figures 3.2b and 3.2f). The degree of openness is associated with the magnitude of the surface irregularity from where it was originated.

Figure 3.11a displays a cross-sectional TEM image of two macroboundaries created by a substrate ridge. Although the macroboundaries in the image are due to the existence of a ridge, they were enhanced by the convex shaped cusps formed by the two adjacent chromium columns at the rim of the ridge. These cusps were reproduced by each individual layer because the coating did not loose the memory of the earlier steps in its growth (see figure 3.11b).

Another type of defects, however, with a much smaller length scale, were formed whenever the chromium columns had a strongly faceted top morphology, resulting in deeper and sharper cusps between two adjacent columns. These planar defects propagated from the cusp minimum, but often only through the intermultilayers. They were ceased by the growth of the WC layer. Others had a longer path but never reached the interface with the WC/C multilayers structure (cf. figure 3.8). Chemical information on the defects was extracted from transmitted electron energy filtering images recorded under high-resolution conditions. Figures 3.12a and 3.12b show a carbon image mapping recorded using the C-K edge and the corresponding compositional

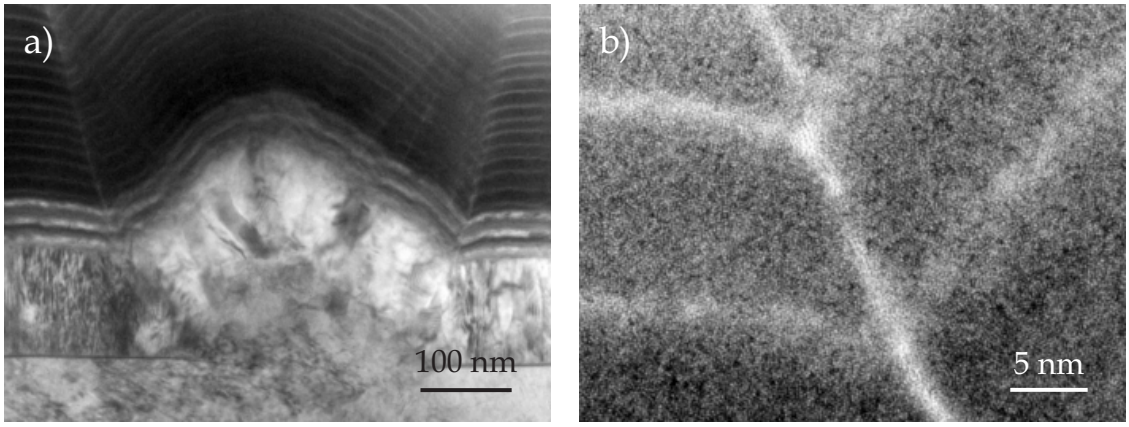

Figure 3.11 (a) *Cross-sectional TEM image of the macroboundaries created by a substrate ridge.* (b) *HRTEM image revealing the defect morphology induced by the convex shaped cusps produced by two adjacent chromium columns at the rim of the ridge.*

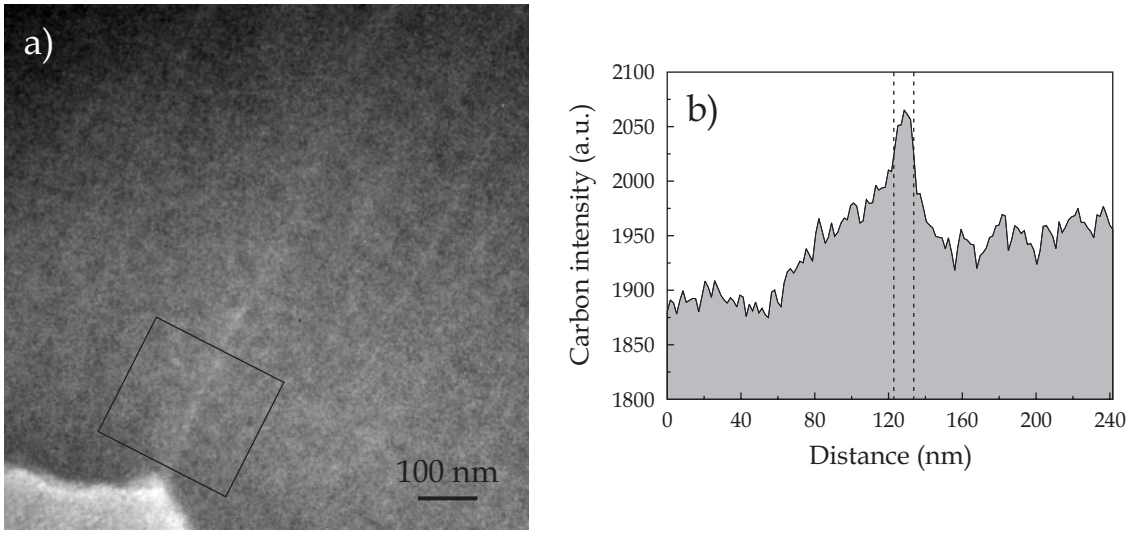

Figure 3.12 (a) *Cross-sectional TEM carbon mapping image of a defect from coated system T1.* (b) *Compositional carbon profile across the defect for an integration width of 100 pixels (214.3 nm). The dash lines delimit the defect width measured from the zero loss image.*

profile taken perpendicular to the defect. The width of integration perpendicular to the resulting profile is a trade-off between resolution and noise. However, a good compromise was obtained by a 100 pixel width (100 pixel equals 214.5 nm). The carbon compositional profile demonstrates that there is enrichment along the defect, which must be caused by carbon segregation during the deposition process. Therefore, it is concluded that the macroboundaries and planar defects are composed by the lower mass-thickness material present in the coating. The reduced path of the planar defects is related to the non-existence of free carbon in the WC layer to stabilise their propagation.

3.6 CONCLUSIONS

In this chapter, the microstructure of WC/C coatings deposited on stainless steel and tool steel has been revealed. The main characteristics are the following:

- The interfacial region between the crystalline steel substrate and the columnar chromium consists of an amorphous high-atomic-density phase;
- The coating structure is constituted by a body centred cubic chromium columnar interlayer, amorphous intermultilayer of WC and carbon, an amorphous WC layer, and finally the amorphous interlaminar WC/C structure;
- One of the differences between the coatings is the thickness of a ribbon with a higher tungsten concentration after the intermultilayers. This ribbon is employed to improve the load capacity of the coating;
- Although the coatings are found to be primarily amorphous, crystalline particles are present, namely, nano-polycrystalline chromium carbides in the carbon layers of the intermultilayers, cubic β-WC_{1-x} in the WC interlayer, and clusters of cubic β-WC_{1-x} phase in the WC lamellae of the interlaminar WC/C;
- Defects structures were generated by the presence of substrate surface irregularities and by the top morphology of the chromium columns. Both

types of defects are mainly composed of carbon. It is given evidence that the presence of a WC interlayer is beneficial for defect truncation because of the non-existence of free carbon to stabilise their propagation.

References

1. A. Erdemir, G.R. Fenske, R.A. Erck, Surf. Coatings Technol. **43-44**, 588 (1990).
2. J.-P. Hirvonen, J. Koskinen, J.R. Jervis, M. Nastasi, Surf. Coatings Technol. **80**, 139 (1996).
3. A. Raveh, L. Martinu, H.M. Hawthorne, M.R. Wertheimer, Surf. Coatings Technol. **58**, 45 (1993).
4. J. Franks, K. Enke, A. Richardt, Metals and Materials, 695 (1990).
5. Y. Liu, A. Erdemir, E.I. Meletis, Surf. Coatings Technol. **82**, 48 (1996).
6. E.G. Spencer, P.H. Schmidt, D.C. Joy, F.J. Sansalone, Appl. Phys. Lett. **129**, 118 (1976).
7. H. Tsai, D.B Bogy, J. Vac. Sci. Technol. A **5**, 3287 (1987).
8. M. Ham, K.A. Lou, Vac. Sci. Technol. A **8**, 2143 (1990).
9. O. Wänstrand, M. Larsson, P. Hedenqvist, Surf. Coatings Technol. **111**, 247 (1999).
10. J. Güttler, J. Reschke, Surf. Coatings Technol. **60**, 531 (1993).
11. A. Matthews, S.S. Eskildesn, Diamond and Related Materials **3**, 902 (1994).
12 A.J. Thornton, Thin Solid Films **40**, 335 (1977).
13 A. Raveh, L. Martinu, S.C. Gujrathi, J.E. Klemberg-Sapieha, M.R. Wertheimer, Surf. Coatings Technol. **53**, 275 (1992).
14. J.W. Edington, *Interpretation of Transmission Electron Micrographs*, MacMillan, London, (1975).
15 J.C. Angus, F. Jansen, J. Vac. Sci. Technol. A **6**, 1778 (1988).
16 J. Robertson, Adv. in Physics **35**, 317 (1986).
17 D.A. Anderson, Philos. Mag. **35**, 17 (1977).
18. A.J. Thornton, J. Vac. Sci. Technol. A **4**, 3059 (1986).
19. P. Ramanlal, L.M. Sander, Physical Review Letters **54**, 1828 (1985).
20. L.E. Toth, *Transition Metal Carbides and Nitrides*, Academic Press, New York, (1971).
21. J.W. Patten, Thin Solid Films **63**, 121 (1979).

APPENDIX 3.1

Structure and dimensions of the coated systems

		System S1	System S2	System T1
Substrate material		Stainless steel	Stainless steel	Tool steel
Chromium layer (nm)		205	120	205
Intermultilayers (nm)	Thickness	93	50	93
	Periodicity	15.5	–	15.5
Amorphous WC layer (nm)		200	–	200
WC/C multilayers (nm)	Thickness	2750	2600	2360
	WC layer	6	13	6
	C layer	2	2.5	2